Lattice dynamics and the nature of structural transitions in organolead halide perovskites

Riccardo Comin, Michael K. Crawford, Ayman H. Said, Norman Herron, William E. Guise, Xiaoping Wang, Pamela S. Whitfield, Ankit Jain, Xiwen Gong, Alan J. H. McGaughey, and Edward H. Sargent

Phys. Rev. B **94**, 094301 — Published 9 September 2016

DOI: 10.1103/PhysRevB.94.094301

Lattice dynamics and the nature of structural transitions in organolead halide perovskites

Riccardo Comin,[1] Michael K. Crawford,[2] Ayman Said,[3] Norman Herron,[2] William E. Guise,[2] Xiaoping Wang,[4] Pamela S. Whitfield,[4] Ankit Jain,[1] Xiwen Gong,[1] Alan J. H. McGaughey,[5] and Edward H. Sargent[1]

[1]*Department of Electrical and Computer Engineering, University of Toronto. 10 Kings College Road, Toronto, Ontario, M5S 3G4, Canada*
[2]*DuPont Central Research and Development, Wilmington, Delaware 19880-0400, United States*
[3]*Advanced Photon Source, Argonne National Lab, Argonne, Illinois 60439, United States*
[4]*Chemical and Engineering Materials Division, Oak Ridge National Laboratory, Oak Ridge, Tennessee 37831, United States*
[5]*Mechanical Engineering Department, Carnegie Mellon University, Pittsburgh, Pennsylvania 15213, United States*

(Dated: July 25, 2016)

Organolead halide perovskites are a family of hybrid organic-inorganic compounds whose remarkable optoelectronic properties have been under intensive scrutiny in recent years. Here we use inelastic X-ray scattering to study low-energy lattice excitations in single crystals of methylammonium lead iodide and bromide perovskites. Our findings confirm the displacive nature of the cubic-to-tetragonal phase transition, which is further shown, using neutron and x-ray diffraction, to be close to a tricritical point. Lastly, we detect quasistatic symmetry-breaking nanodomains persisting well into the high-temperature cubic phase, possibly stabilized by local defects. These findings reveal key structural properties of these materials, and also bear important implications for carrier dynamics across an extended temperature range relevant for photovoltaic applications.

PACS numbers: Valid PACS appear here

Structural phase transitions and tetragonal symmetry lowering have long been long studied in cubic halide and oxide perovskites [1–4]. The nature of the phase transition is generally understood to be of the displacive type, involving the softening of a zone-edge mode (such as in $CsPbCl_3$, $SrTiO_3$, and $KMnF_3$) or a zone-center mode (such as in $PbTiO_3$) and the consequent frozen-in distortion of the lattice in the low-symmetry phase. This mechanism is accompanied by a change in symmetry which in reciprocal space is signalled by the emergence of a superlattice Bragg reflection at the wavevector where the phonon softening occurs. In hybrid lead halide perovskites, a materials platform which has catalyzed considerable attention in the field of optoelectronics in recent years [5], the crystal structure plays a fundamental role, exerting a direct feedback on the electronic structure and the bandgap [6–8]. The resulting bandstructure and associated optical response are in turn crucial for photovoltaic and light emission applications, where spectral tunability is key for device performance and versatility. The influence of the structural changes on the performance of perovskite-based solar devices has been explored previously from both an experimental [9] and a theoretical [10] viewpoint, across an extended temperature range relevant to photovoltaic functionality. Phenomenologically, it has been observed that the cubic-to-tetragonal phase transition has little effect on device performance, a finding that was later elucidated using *ab initio* molecular dynamics simulations. This investigation revealed that on a sub-ps timescale the carriers still experience a slightly distorted (i.e. non-cubic) local environment, not dissimilar to that of the room-temperature tetragonal phase, thus lifting any discontinuity in the bandstructure and corresponding electrodynamics. A question then arises as to whether the local deviations from the cubic structure in the high-temperature phase are purely dynamic, or whether there is a static component, quenched by the presence of symmetry-breaking localized defects.

In order to assess such a scenario, in the present study we investigate the lattice dynamics of methylammonium ($MA = CH_3NH_3$) lead iodide ($MAPbI_3$) and bromide ($MAPbBr_3$) along the high-symmetry direction of the cubic phase of these compounds. $MAPbI_3$ crystallizes at room temperature in the tetragonal structure (space group $I4/mcm$) whereas $MAPbBr_3$ is found in the cubic phase (space group $Pm\bar{3}m$) and both compounds undergo a cubic-to-tetragonal first-order structural transition at $T_c = 327.5\,\mathrm{K}$ and $236.9\,\mathrm{K}$, respectively [11]. With the intent of clarifying the mechanistic details of the cubic-to-tetragonal phase transition, we use x-ray powder diffraction and neutron scattering to analyze the changes in lattice symmetry via the superlattice Bragg reflection, which serves as order parameter for the tetragonal structure. Additionally, we use inelastic X-ray scattering (IXS) to measure the dynamical structure factor as a function of momentum and energy in an extended portion of reciprocal space, and in the meV energy range. For these measurements, we synthesized crystals of $MAPbI_3$ and $MAPbBr_3$ using the inverse temperature crystallization method described in Ref. 12 and 13. X-ray and neutron experiments have been performed at the superlattice reflection $(3/2, 1/2, 1/2)$, defined with respect to the cubic unit cell. In order to map out the complete phonon dispersion with IXS, we focused on reciprocal space di-

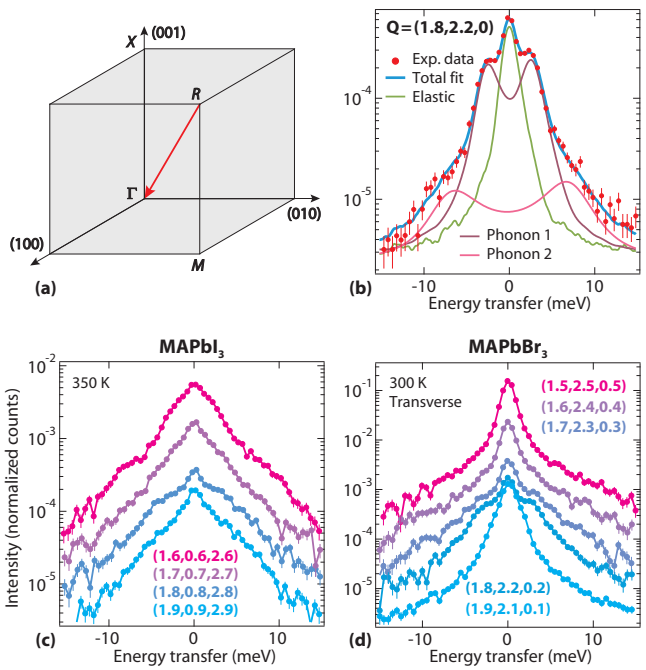

FIG. 1. (a) Reciprocal space coordinates for the cubic structure, with high-symmetry points highlighted. The red arrow defines the trajectory followed for the measurements shown in panels (c,d). (b) Single IXS scan from $MAPbBr_3$ showing a representative overall fit profile and its decomposition into elastic line and phonon sidebands. (c,d) A series of inelastic scans (scattered intensity vs. energy transfer) of $MAPbI_3$ (c) and $MAPbBr_3$ (d) at selected wavevectors along the path defined in (a).

rections connecting the Brillouin zone center point Γ [with wavevector $\mathbf{Q}_\Gamma = (H, K, L)$] to the zone edge high-symmetry points of the cubic phase, namely X [$\mathbf{Q}_X = (H+1/2, K, L)$], M [$\mathbf{Q}_M = (H+1/2, K+1/2, L)$], and R [$\mathbf{Q}_R = (H+1/2, K+1/2, L+1/2)$] [14]. The location of these special points within the Brillouin zone of the high-temperature phase is shown in Fig. 1(a). The red arrow defines the high-symmetry cut $R \rightarrow \Gamma$, for which a series of scans of the scattered intensity vs. energy transfer is shown at selected wavevectors for $MAPbI_3$ [Fig. 1(c)] and $MAPbBr_3$ [Fig. 1(d)]. All the IXS scans presented in this study have been measured in the cubic phase, at $T = 350$ K and 300 K for $MAPbI_3$ and $MAPbBr_3$, respectively.

The IXS profiles have been analyzed using a functional form which incorporates a sharp (δ-function) elastic line together with a damped-harmonic-oscillator (DHO) functional form [15]:

$$I_{\mathrm{DHO}}(\mathbf{Q},\omega) = I_{\mathrm{el}} \cdot \delta(\omega) + I_{\mathrm{inel}} \cdot \left[\frac{\Omega_{\mathbf{Q}}^2 \Gamma_{\mathbf{Q}}}{\left(\omega^2 - \Omega_{\mathbf{Q}}^2\right)^2 + \omega^2 \Gamma_{\mathbf{Q}}^2} \right], \quad (1)$$

where ω is the photon angular frequency, $\Omega_{\mathbf{Q}}$ and $\Gamma_{\mathbf{Q}}$ are the momentum-dependent phonon frequency and damping (inverse lifetime), and I_{el} and I_{inel} are the intensities of the elastic and inelastic terms, respectively. The final model function applied to the analysis of the experimental data is obtained after multiplication of Eq. 1 by the Bose factor $[n(\omega)+1]$ to account for the temperature-dependent phonon population [$n(\omega)$ being the Bose-Einstein function] and subsequent convolution with the instrument resolution function (see also Supplemental Material). An example of the fit profile based on this model function is shown in Fig. 1(b), where two sets of phonon sidebands can be resolved, together with the central elastic line. By applying this analysis to a complete dataset of IXS experimental profiles, we have extracted the phonon dispersions in $MAPbI_3$ [Fig. 2(a)] and $MAPbBr_3$ for longitudinal [Fig. 2(b)] and transverse modes [Fig. 2(c)], along the $\Gamma \rightarrow X$ (red), $\Gamma \rightarrow M$ (green), and $\Gamma \rightarrow R$ (blue) directions. From numerical fits of the experimental data to Eq. 1, we have derived both the phonon frequency (markers) and broadening (vertical bars). The number of branches that we could resolve depends on the counting statistics and varies with the wavevector, but in all cases is limited by the range of energy transfer (± 15 meV). All the modes detected in our measurements corresponds to low-energy excitations of the corner-sharing PbX_3 (X = I, Br) network, while the methylammonium internal vibrations generally appear at higher energies, although the translational and librational modes are found in the 10-20 meV energy range [16, 17]. While it is possible that multiple modes are lumped together within individual fitted peaks, the broad energy linewidths observed at various momenta might also indicate short phonon lifetimes, as recently observed using Raman spectroscopy [18]. The experimental phonon frequencies are compared to the theoretical vibrational bandstructure calculated using density functional theory in the frozen-phonon approximation [dispersions are overlaid in Figs. 2 and are in close agreement with those reported in Ref. 17]. In addition, the highest zone-center optical mode in $MAPbI_3$ is found at 7-7.5 meV, consistent with recent findings from a Raman/IR study [19]. Additionally, we note that the phonons become overdamped at the R-point (this is particularly evident for $MAPbBr_3$), where numerical calculations predict an instability as signalled by the imaginary mode frequency, consistent with a displacive structural transition triggered by phonon condensation at the zone-corner. A closer inspection of the longitudinal (LA) and transverse acoustic (TA) phonon dispersions in the vicinity of the Γ-point (along the $\Gamma \rightarrow X$ direction) yields an estimate of the sound speed, which is a relevant quantity with a direct impact on the carrier mobility μ via electron-phonon coupling [20]. This analysis indicates a longitudinal (shear) sound speed of $v_l = 2714 \pm 650$ m/s ($v_s = 990 \pm 150$ m/s) in $MAPbBr_3$, while in $MAPbI_3$ this procedure is hindered by the inabil-

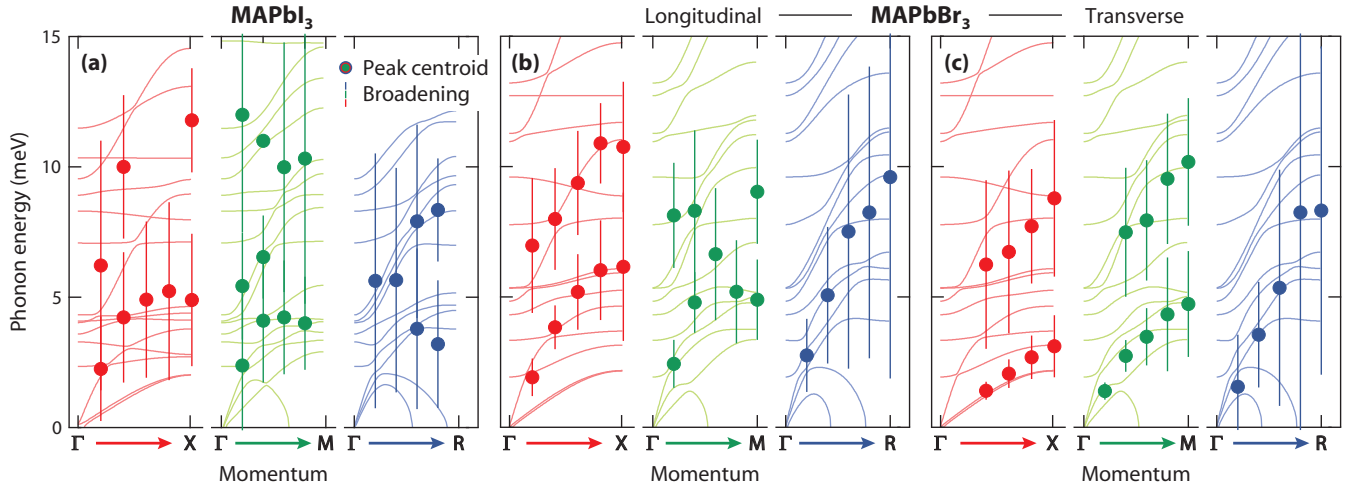

FIG. 2. (a) Experimental phonon dispersions (and calculated phonon bands overlaid) in $MAPbI_3$ along the three high-symmetry direction of the cubic phase, namely $\Gamma \rightarrow X$ (red, left), $\Gamma \rightarrow M$ (green, center), and $\Gamma \rightarrow R$ (blue, right). Longitudinal and transverse modes are mixed due to the scattering geometry adopted for $MAPbI_3$. (b,c) Experimental phonon dispersions (and calculated phonon bands overlaid) in $MAPbBr_3$ for longitudinal (b) and transverse (c) modes. Note: vertical bars reflect the experimental linewidth of phonon peaks and not the uncertainty on phonon frequency.

ity to separate the LA and TA branches, which are mixed in due to the experimental geometry. However, from the calculated phonon bands we obtain $v_l \sim 3270\,\mathrm{m/s}$ and $v_s \sim 970\,\mathrm{m/s}$. The sound speed measured using IXS slightly underestimates the sound speed in the hydrodynamic regime ($\sim 1200\,\mathrm{m/s}$) as measured using picosecond acoustic dynamics [21]. Further, these values suggest that the electron-phonon scattering rate τ^{-1} from acoustic modes, which is inversely proportional to the sound speed ($\tau^{-1} \propto v^2$, see Ref. 22), is slightly higher in $MAPbI_3$ and $MAPbBr_3$. However, it was recently pointed out that scattering of electrons from optical phonons is the dominant mechanism behind electron transport in these materials [18, 22, 23], likely explaining the long carrier lifetimes and diffusion lengths observed in high-quality crystals of hybrid halide perovskites [24].

In the second part of our study we examined the momentum fingerprints of the cubic-to-tetragonal structural transition and how the lowering of the lattice symmetry is unfolded in reciprocal space.

The nature of the cubic-tetragonal phase transition was also investigated using single crystal neutron diffraction at the ORNL Spallation Neutron Source's TOPAZ instrument [25] for a deuterated $MAPbI_3$ crystal (d_6-$MAPbI_3$) and synchrotron X-ray powder diffraction for a fully hydrogenated polycrystalline sample (h_6-$MAPbI_3$). The intensity of the (3/2 1/2 1/2) superlattice Bragg peak and the tetragonal distortion were measured to evaluate the critical behavior of the phase transition, and the results are shown in Fig. 3. Each set of data was fit to a power law, $I \sim (T_c - T)^{2\beta}$, where the factor of two in the exponent accounts for the fact that the superlattice intensity will scale as the square of the order parameter for the phase transition, where the order parameter is the rotation angle of the PbI_6 octahedra [26].

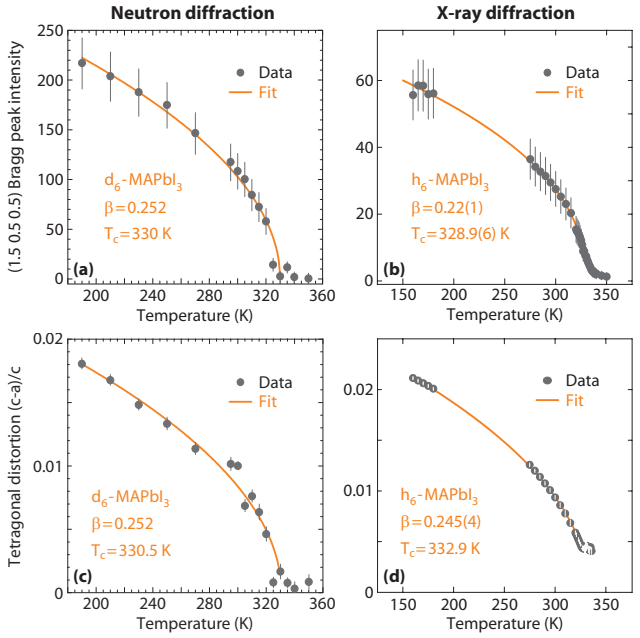

FIG. 3. (a,c) Cubic (3/2 1/2 1/2) superlattice Bragg intensity (a) and tetragonal distortion (c) for single crystal d_6-$MAPbI_3$ measured by neutron diffraction on TOPAZ. (b,d) Cubic (3/2 1/2 1/2) superlattice Bragg intensity and tetragonal distortion for polycrystalline h_6-$MAPbI_3$ measured by X-ray powder diffraction on DND-CAT. Error bars in panel (d) are multiplied by a factor 3 for clarity.

Similarly, the tetragonal strain is a secondary order parameter which is also expected to scale as the square of the order parameter for the phase transition [27]. The values of β vary from 0.249 to 0.28, where the mean-field result for a second-order phase transition is $\beta = 0.5$. The measured values are close to that expected for a tricritical phase transition, $\beta = 0.25$, which occurs at the intersection of lines of first-order and second-order phase transitions [28]. However, the presence of a distinct temperature range of cubic and tetragonal phase coexistence [29], and latent heat in heat capacity measurements [30], are only consistent with a first-order transition, suggesting that these materials are still on the first-order side of the tricritical point.

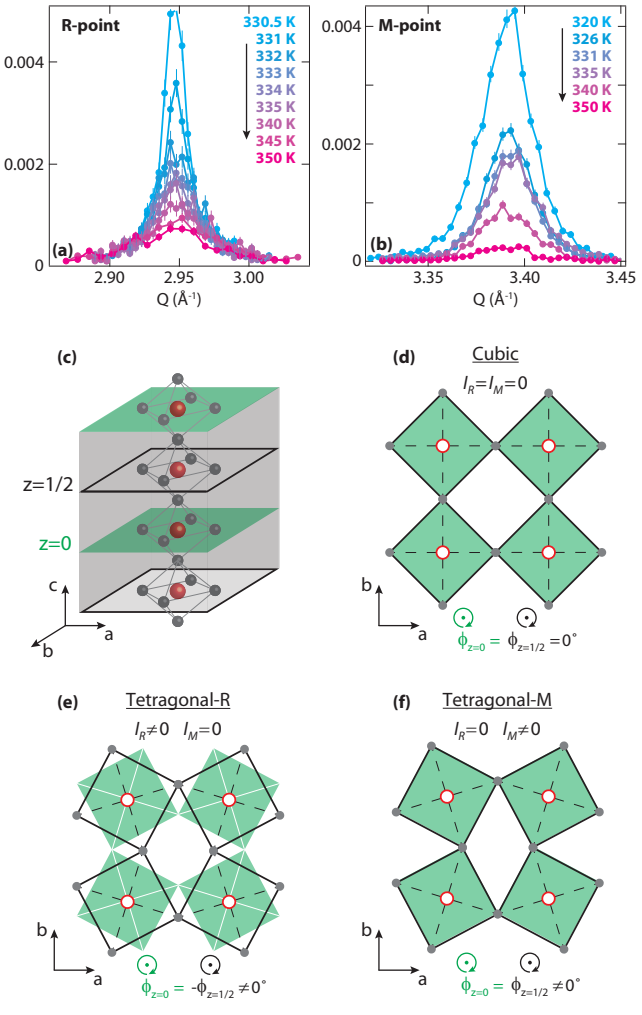

FIG. 4. (a,b) Temperature-dependent momentum scans of $MAPbI_3$ at the R- (a) and M-point (b) above the cubic-to-tetragonal phase transition temperature. (c-f) Side view of the crystal structure (c), and top view along c-axis highlighting the different octahedral rotation motifs for the cubic (undistorted) phase (d), tetragonal-R phase (e), and tetragonal-M phase (f). Note that the two tetragonal phases have different unit cells (the one of tetragonal-R structure is doubled along the c-axis) and their order parameters are represented by the Bragg intensity at R- and M-point, respectively.

Furthermore, we have performed IXS scans in momentum space across the R- and M-points in $MAPbI_3$, as a function of temperature above the phase transition [Figs. 4(a) and (b)]. More specifically, we have scanned reciprocal space by sweeping the detector (and therefore the scattering) angle while in energy-resolved mode, i.e. collecting only the elastically scattered light at $\omega = 0$ and at low momentum resolution (0.01 $Å^{-1}$) to maximize the sensitivity to weak scattering signals. Most importantly, the high energy resolution allows us to separate the elastic (quasistatic) component from the thermal diffuse scattering, which is inelastic in nature and cannot be avoided in energy-integrated measurements such as neutron or X-ray diffraction, discussed above. At variance with previous reports [31], we find that the (elastic) scattered intensity at the R-point does not vanish above T_c, but persists up to 20 K away from the transition temperature, as shown in Fig. 3(a) (a similar behavior is found in $MAPbBr_3$, see Supplemental Material). In $MAPbI_3$ we also detect weaker reflections at the M-point [Fig. 3(b)], which suggests that, alongside the dominant lattice symmetry and its representative Bragg signatures, there are small regions with short-range-ordered puddles locally breaking cubic symmetry. Since our data at $\omega = 0$ only reflect the static scattering, they demonstrate the existence of symmetry-breaking nanopuddles well above the thermodynamic structural transition temperature, in analogy with the phenomenology of the central peak in $SrTiO_3$ [32, 33]. The associated temperature evolution of the forbidden superlattice reflection intensities (which in the cubic phase are $\sim$ 2 orders of magnitude weaker than the allowed R-point Bragg reflection below T_c) and correlation lengths (see Supplemental Material) suggests that these nanoislands initially nucleate around defects that break cubic symmetry and progressively grow in size coalescing into long-range ordered structures near and below the phase transition. The formation of these cubic-symmetry-breaking domains therefore precedes the complete renormalization of the phonon frequency and the concomitant condensation of the phonon mode into a static distortion. These two phenomena are *a priori* independent, and while the phonon softening mechanism is driven by a native instability of the cubic lattice, the short-ranged nanodomains likely reflect the nature of the symmetry-breaking defects, previously investigated [34, 35]. This likely explains why we observe scattering intensity also at the M-point, where no frozen-in phonon modes should be expected altogether.

In conclusion, the present study confirms the existence of a lattice instability at the R-point, and elucidates the tricritical nature of the cubic-to-tetragonal phase transition. In addition, we uncover the presence of static short-ranged order well above the structural transition

and in the temperature range relevant for photovoltaic operation.

Acknowledgements

A portion of this research at Oak Ridge National Laboratorys Spallation Neutron Source was sponsored by the Scientific User Facilities Division, Office of Basic Energy Sciences, U. S. Department of Energy. Portions of this work were performed at the DuPont-Northwestern-Dow Collaborative Access Team (DND-CAT) located at Sector 5 of the Advanced Photon Source (APS). DND-CAT is supported by Northwestern University, E.I. DuPont de Nemours & Co., and The Dow Chemical Company. This research used resources of the Advanced Photon Source, a U.S. Department of Energy (DOE) Office of Science User Facility operated for the DOE Office of Science by Argonne National Laboratory under Contract No. DE-AC02-06CH11357.

[1] G. Shirane and S. Hoshino, Journal of the Physical Society of Japan **6**, 265 (1951), http://dx.doi.org/10.1143/JPSJ.6.265.

[2] Y. Fujii, S. Hoshino, Y. Yamada, and G. Shirane, Physical Review B **9**, 4549 (1974).

[3] S. R. Andrews, Journal of Physics C: Solid State Physics **19**, 3721 (1986).

[4] U. J. Nicholls and R. A. Cowley, Journal of Physics C: Solid State Physics **20**, 3417 (1987).

[5] S. D. Stranks and H. J. Snaith, Nature Nanotechnology **10**, 391 (2015).

[6] J. H. Noh, S. H. Im, J. H. Heo, T. N. Mandal, and S. I. Seok, Nano Letters **13**, 1764 (2013).

[7] E. Mosconi, A. Amat, M. K. Nazeeruddin, M. Grtzel, and F. De Angelis, The Journal of Physical Chemistry C **117**, 13902 (2013).

[8] R. Comin, G. Walters, E. S. Thibau, O. Voznyy, Z.-H. Lu, and E. H. Sargent, Journal of Materials Chemistry C **3**, 8839 (2015).

[9] H. Zhang, X. Qiao, Y. Shen, T. Moehl, S. M. Zakeeruddin, M. Grtzel, and M. Wang, Journal of Materials Chemistry A **3**, 11762 (2015).

[10] C. Quarti, E. Mosconi, and F. De Angelis, Chemistry of Materials **26**, 6557 (2014).

[11] A. Poglitsch and D. Weber, The Journal of Chemical Physics **87**, 6373 (1987).

[12] J. M. Kadro, K. Nonomura, D. Gachet, M. Grtzel, and A. Hagfeldt, Scientific Reports **5**, 11654 (2015).

[13] M. I. Saidaminov, A. L. Abdelhady, B. Murali, E. Alarousu, V. M. Burlakov, W. Peng, I. Dursun, L. Wang, Y. He, G. Maculan, A. Goriely, T. Wu, O. F. Mohammed, and O. M. Bakr, Nature Communications **6** (2015), 10.1038/ncomms8586.

[14] Here, H, K, and L are integer indices, which are also used to label the reciprocal lattice location where measurements were perfomed.

[15] B. Fåk and B. Dorner, Physica B: Condensed Matter **234236**, 1107 (1997), proceedings of the First European Conference on Neutron Scattering.

[16] C. Quarti, G. Grancini, E. Mosconi, P. Bruno, J. M. Ball, M. M. Lee, H. J. Snaith, A. Petrozza, and F. D. Angelis, The Journal of Physical Chemistry Letters **5**, 279 (2014).

[17] F. Brivio, J. M. Frost, J. M. Skelton, A. J. Jackson, O. J. Weber, M. T. Weller, A. R. Goi, A. M. A. Leguy, P. R. F. Barnes, and A. Walsh, Physical Review B **92**, 144308 (2015).

[18] A. M. A. Leguy, A. R. Goi, J. M. Frost, J. Skelton, F. Brivio, X. Rodrguez-Martnez, O. J. Weber, A. Pallipurath, M. I. Alonso, M. Campoy-Quiles, M. T. Weller, J. Nelson, A. Walsh, and P. R. F. Barnes, arXiv:1606.01841 [cond-mat, physics:physics] (2016), arXiv: 1606.01841.

[19] M. A. Prez-Osorio, R. L. Milot, M. R. Filip, J. B. Patel, L. M. Herz, M. B. Johnston, and F. Giustino, The Journal of Physical Chemistry C (2015), 10.1021/acs.jpcc.5b07432.

[20] S. Takagi, A. Toriumi, M. Iwase, and H. Tango, IEEE Transactions on Electron Devices **41**, 2363 (1994).

[21] Z. Guo, S. J. Yoon, J. S. Manser, P. V. Kamat, and T. Luo, The Journal of Physical Chemistry C **120**, 6394 (2016).

[22] A. Filippetti, A. Mattoni, C. Caddeo, M. I. Saba, and P. Delugas, Physical Chemistry Chemical Physics **18**, 10.1039/C6CP01402J.

[23] A. D. Wright, C. Verdi, R. L. Milot, G. E. Eperon, M. A. Prez-Osorio, H. J. Snaith, F. Giustino, M. B. Johnston, and L. M. Herz, Nature Communications **7**, 0 (2016).

[24] D. Shi, V. Adinolfi, R. Comin, M. Yuan, E. Alarousu, A. Buin, Y. Chen, S. Hoogland, A. Rothenberger, K. Katsiev, Y. Losovyj, X. Zhang, P. A. Dowben, O. F. Mohammed, E. H. Sargent, and O. M. Bakr, Science **347**, 519 (2015).

[25] A. J. Schultz, M. R. V. Jørgensen, X. Wang, R. L. Mikkelson, D. J. Mikkelson, V. E. Lynch, P. F. Peterson, M. L. Green, and C. M. Hoffmann, Journal of Applied Crystallography **47**, 915 (2014).

[26] Y. Kawamura, H. Mashiyama, and K. Hasebe, Journal of the Physical Society of Japan **71**, 1694 (2002).

[27] J. C. Slonczewski and H. Thomas, Phys. Rev. B **1**, 3599 (1970).

[28] J.-C. Toledano and P. Toledano, *The Landau theory of phase transitions* (1987).

[29] P. Whitfield, N. Herron, W. Guise, K. Page, Y. Q. Cheng, and M. Crawford, submitted (2016) (2016).

[30] N. Onoda-Yamamuro, T. Matsuo, and H. Suga, Journal of Physics and Chemistry of Solids **51**, 1383 (1990).

[31] M. T. Weller, O. J. Weber, P. F. Henry, A. M. D. Pumpo, and T. C. Hansen, Chemical Communications **51**, 4180 (2015).

[32] M. Holt, M. Sutton, P. Zschack, H. Hong, and T.-C. Chiang, Physical Review Letters **98** (2007), 10.1103/PhysRevLett.98.065501.

[33] H. Hong, R. Xu, A. Alatas, M. Holt, and T.-C. Chiang, Physical Review B **78**, 104121 (2008).

[34] A. Buin, P. Pietsch, J. Xu, O. Voznyy, A. H. Ip, R. Comin, and E. H. Sargent, Nano Letters **14**, 6281 (2014).

[35] A. Buin, R. Comin, J. Xu, A. H. Ip, and E. H. Sargent, Chemistry of Materials **27**, 4405 (2015).